CrystEngComm

ROYAL SOCIETY OF CHEMISTRY

HIGHLIGHT

View Article Online
View Journal | View Issue

Cite this: *CrystEngComm*, 2025, **27**, 7601

Benzothienobenzothiophene: recent uses as a transistor material and derivatization for adding new features in device functions

Tomofumi Kadoya, *[a] Takuto Imai,[b] Hiroki Sano,[b] Yuki Kobayashi,[b] Hikaru Takashima,[b] Miyabi Shirakura,[b] Hirotaka Kojima, [c] Masahiro Yamamoto [a] and Keishiro Tahara *[d]

Received 17th September 2025,
Accepted 23rd October 2025

DOI: 10.1039/d5ce00904a

rsc.li/crystengcomm

Over the past two decades, benzothienobenzothiophene (BTBT) derivatives have been widely studied as excellent organic transistor materials. Recent research across various diverse fields has advanced BTBT-based electronics to a new stage of development. This review first outlines the chemical properties of BTBT molecules and introduces representative research on transistors since 2022, including studies on material development and improvements in device manufacturing processes. Subsequently, it presents various applications in other organic electronics such as solar cells, thermoelectric converters, and light-emitting elements, whose properties are mainly based on π-extension, donor–acceptor structures, coordination chemistry, and emerging concepts in light emission such as aggregation-induced emission and thermally activated delayed fluorescence. The review findings can help promote an understanding of the functional potential of BTBT and support the future development of advanced organic materials.

1 Introduction

Organic field-effect transistors (OFETs), particularly those used in switching and memory applications, have seen significant advancements in recent decades owing to their potential for flexible, low-cost, and large-scale electronics.[1–6] These transistors are also used to study the charge transport properties of molecular solids using field effects.[7] Generally, organic semiconductors can be classified as small molecules and polymers. The physical and chemical properties of small organic molecules can be precisely controlled by changing their molecular structures. Specifically, large interactions between molecules in solids are important for efficient charge transport. The realisation of molecular arrangements with multidimensional electronic structures is crucial for the development of high-performance transistors; accordingly, research has been increasingly focused on controlling and predicting their crystal structures based on the shape of the molecules.[8–10]

In the early days of OFET research, pentacenes, oligothiophenes, and phthalocyanines were extensively used.[11] Recently, heteroarenes and aromatic fusions of thiophene and benzene rings have become the dominant structures in p-type transistor materials. Liquid-crystalline molecule [1]benzothieno[3,2-*b*]benzothiophene (BTBT) derivatives have been reported as a promising class of heteroarene semiconductors for OFETs.[12–14] Since then, semiconductor development using heteroarenes, particularly the benzothiophene moiety, has advanced rapidly.

Most BTBT derivatives with substituents at positions 2 and 7 are excellent organic semiconductors with high mobility.[15,16] Although these BTBT derivatives have an extended π-electron molecular structure, similar to common acene compounds, the highest occupied molecular orbital (HOMO) energy levels are deeper than those of acenes with the same number of aromatic rings owing to the insertion of thiophene moieties. Their deep HOMO levels prevent BTBT derivatives from being easily oxidised. Therefore, their thin-film transistors operate stably under ambient conditions without degradation. Furthermore, sulfur atoms are more effective than carbon atoms in strengthening the intermolecular overlap of the molecular orbitals. BTBT derivatives are considered pivotal to the advancement of p-channel organic transistors. Recently, substances containing the BTBT skeleton have been applied not only to transistors, but also in various other fields.[17] This review highlights the chemical properties of BTBT and provides examples of transistor materials, metal complexes, and other functional materials containing the BTBT skeleton.

[a] *Department of Chemistry, Konan University, 8-9-1 Okamoto, Higashinada, Kobe 658-8501, Japan. E-mail: tkadoya@konan-u.ac.jp*
[b] *Graduate School of Natural Science, Konan University, 8-9-1 Okamoto, Higashinada, Kobe 658-8501, Japan*
[c] *National Institute of Technology (KOSEN), Maizuru College 234 Shiroya, Maizuru, Kyoto 625-8511, Japan*
[d] *Faculty of Engineering and Design, Kagawa University, 2217-20, Hayashi-cho, Takamatsu, Kagawa 761-0396, Japan. E-mail: tahara.keishiro@kagawa-u.ac.jp*

2 Chemical properties of BTBT

Hole transport in p-channel semiconductors is primarily realised by the HOMO. Although p-channel transistors can operate in air, some compounds are affected and degraded by atmospheric water and oxygen. The stability of semiconductors with respect to water can be estimated from the reaction potentials of water reduction and oxidation. Based on the standard hydrogen electrode (SHE), protons are reduced to H_2 by the reaction $2H^+(aq) + 2e^- \rightarrow H_2(g)$, when $E_{redox} < 0$ V *vs.* SHE. In contrast, water undergoes the oxidation reaction $2H_2O \rightarrow O_2 + 4H^+ + 4e^-$, when $E_{redox} > 1.23$ V *vs.* SHE, producing oxygen and protons. Therefore, the potential range of $0\ V < E_{redox} < 1.23$ V is the region in which water is stable. These redox potentials involve proton shifts with pH. The pH dependence of the potential using the Nernst equation is expressed as follows:

$$E\ (vs.\ \text{SHE}) = -59\ \text{mV} \times \text{pH}.$$

At neutral pH (pH = 7), the potential must be shifted by $E = -0.41$ V; therefore, the resulting neutral water stability field is $-0.41\ V < E_{redox}\ (vs.\ \text{SHE}) < 0.82$ V.

Considering the potential of the saturated calomel electrode (SCE), $E\ (vs.\ \text{SHE}) = E\ (vs.\ \text{SCE}) + 0.242$ V; therefore, $E\ (vs.\ \text{SCE or SHE})$ is converted to units of eV using $-E = E_{redox}\ (vs.\ \text{SCE}) + 4.44\ V = E_{redox}\ (vs.\ \text{SHE}) + 4.198$ V.[18] Thus, the energy level at which water exists stably corresponds to approximately $-3.8\ eV > E > -5.0$ eV. This potential estimate is based on a simple four-electron, one-step mechanism of the water-splitting reaction; however, various models exist for this reaction,[19] each affecting the redox potential for oxygen evolution. In particular, the overpotential cannot be ignored; however, its value varies depending on the measurement conditions, rendering accurately estimating the stable region of water challenging.

Strong electron donors with $E > 5.0$ eV, such as tetrathiafulvalene derivatives (4.8–5.0 eV), are easily oxidised by oxygen in air, resulting in 'normally on' operations.[20–23] Long-term air stability is also not expected. Conversely, weak electron donors such as BTBT, picene, and phenacene derivatives with $E_{HOMO} = 5.6$–5.8 eV exhibit transistor properties with 'normally off', long-term air stability.[24–26]

Oxidation resistance based on this deep HOMO level is one of the characteristics of BTBT. Fig. 1 shows the energy level and shape of the HOMO of each molecule estimated through molecular orbital calculations. The thiophene ring is not a six-membered ring but is supplied with two π-electrons from the sulfur atom and possesses the same aromaticity as the benzene ring. Therefore, polycyclic aromatic hydrocarbons similar to BTBT are tetracene and chrysene. Generally, molecules with kinked or bent benzene rings form more stable compounds with a larger band gap and deeper HOMO levels than those with linearly fused benzene rings and are more resistant to oxidation. This is mainly because of the nature of H–H repulsion in the kinked molecules and has been discussed in detail in theoretical studies.[27]

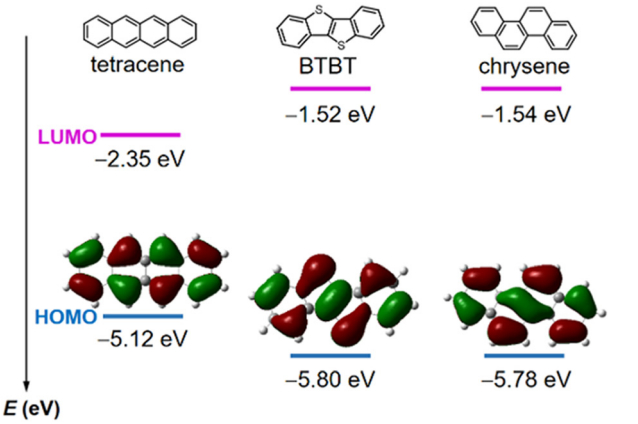

Fig. 1 Calculated energy levels and HOMOs (density functional theory (DFT) calculations, B3LYP/6-311g(d,p) level).

The presence of a thiophene ring inside the fused ring provides an electronic structure closer to a kinked phene-type aromatic hydrocarbon system than to a linearly fused acene-type aromatic hydrocarbon system (Fig. 1). Therefore, the electronic natures of BTBT are more similar to those of chrysene than to those of tetracene. As sulfur has a larger atomic radius than carbon, organic semiconductors containing thiophene rings are considered to have large molecular orbitals. The introduction of sulfur atoms to enhance intermolecular HOMO contributions has been widely used in the development of organic conductors and semiconductors.[28–31]

However, the intramolecular HOMO distribution varies significantly depending on the shape of the molecule. Fig. 2(a) shows the HOMO distributions of thiophene-based molecules. In a normal thiophene ring, the HOMO is not sufficiently localised on the sulfur atom, and nodal planes exist. This property is common for oligothiophenes and thienothiophenes.[32] Numerous studies have reported that

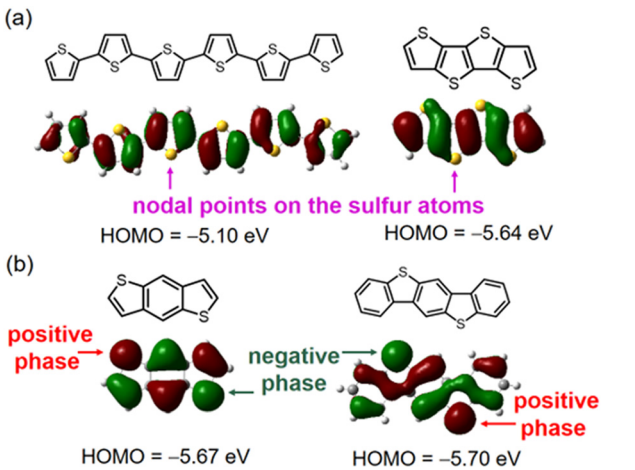

Fig. 2 HOMO distribution of (a) thiophene- and (b) benzodithiophene-based molecules (density functional theory (DFT) calculations, B3LYP/6-311g(d,p) level).

BTBT derivatives often exhibit relatively superior transistor performance compared to oligothiophene derivatives.[33–35] Empirical findings suggest that the localisation of the HOMO on sulfur atoms enhances intermolecular transfer integrals, thereby improving p-channel transistor performance. BTBT exhibits this property and has a large HOMO coefficient for the sulfur atom. In BTBT, the sign (phase) of the HOMO coefficient localised on the sulfur atom is the same in the molecular plane; however, it changes when a benzene ring is fused between the thiophene rings (Fig. 2(b)). The overlap integral between the molecules depends on the molecular-orbital phase differences. Hence, HOMO-coefficient phase differences may also affect the transistor properties, although this has not been investigated in detail yet. Molecules with different HOMO phases on the sulfur atom generally exhibit excellent transistor properties.[36] In organic charge-transfer complexes, thiophene-based oligomers have recently been reported to form crystal orbitals with specific HOMO–LUMO interactions in mixed-stacked charge-transfer complexes, which are effective in improving conductivity.[37] However, this new concept has not yet been applied to organic transistors. In typical organic transistors, the arrangement of semiconductor molecules in a crystal is as important as the electronic properties of a single molecule because the semiconductor layer is mostly formed by molecular assemblies. While rubrene with pitched π stacks is a special case,[38,39] semiconductors that form two-dimensional (2D) carrier paths, such as herringbone and brickwork, tend to exhibit high mobility.[40,41] Organic semiconductors with 2D carrier paths are less susceptible to carrier trapping during charge transport than π stacks, which are one-dimensional electronic structures. The high crystallinity derived from the layered structure is also suitable for single-crystal transistors fabricated *via* solution processing, and the introduction of

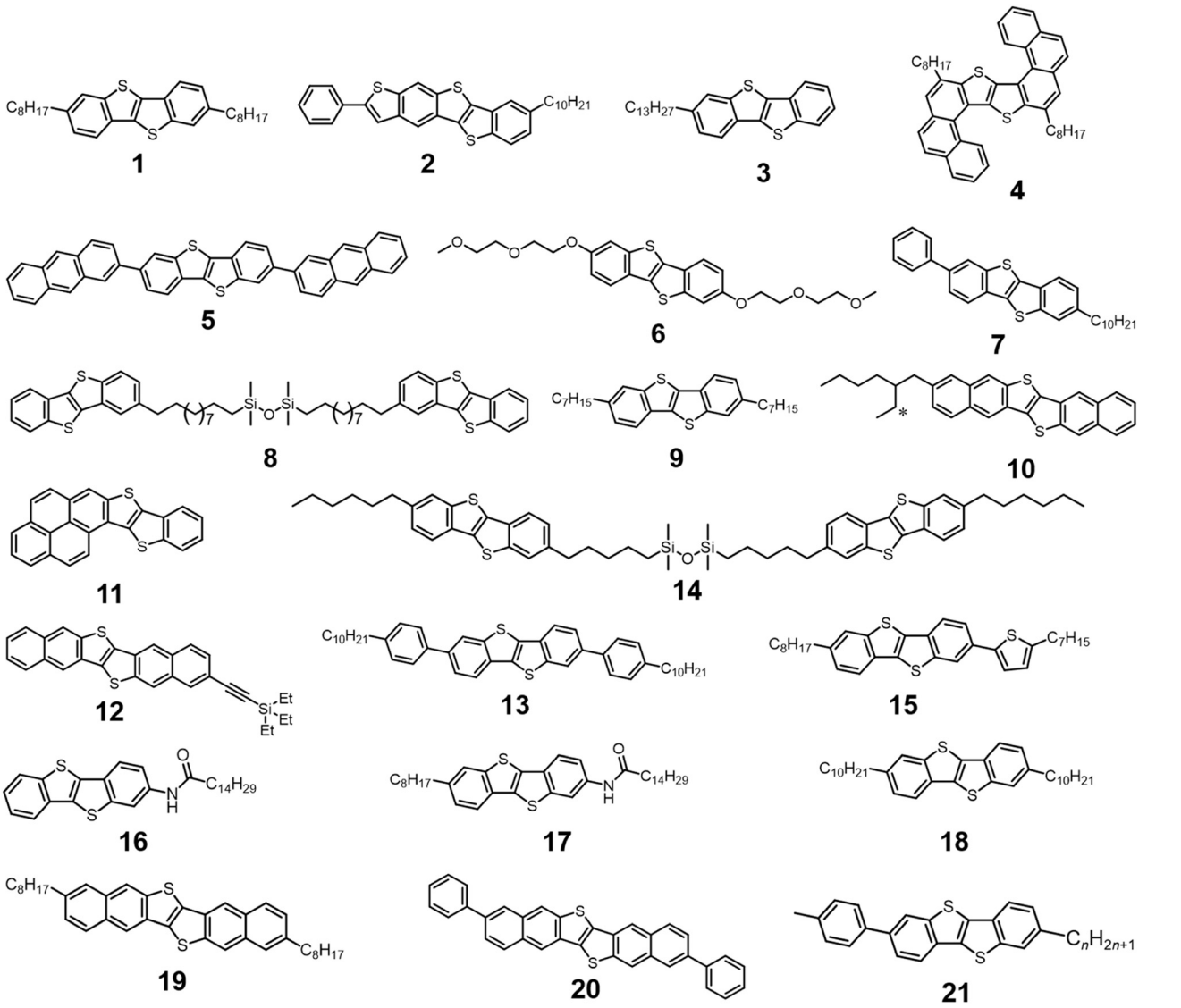

Fig. 3 Molecular structures of BTBT derivatives reported in recent studies.

long-chain alkyl groups at positions 2 and 7 of BTBT facilitates the formation of herringbone arrays. However, the heavy chalcogen substitution method has not been widely applied to BTBT derivatives. This may be because the heavy chalcogen substitution of sulfur to enhance the intermolecular overlap changes the molecular arrangement from herringbone to a π stack.[42,43] As mentioned earlier, research on BTBT derivatives has been progressing, as it is easy to create 2D electronic structures in crystals, and the electronic properties of a single molecule are advantageous for transistors.

3 Organic transistors based on BTBT moieties

Fig. 3 and Table 1 list the relevant material development studies on the BTBT moiety since 2022.[44–83] This review analysed the research trends and found that many studies have used C8-BTBT, a typical BTBT-based semiconductor, and focused on the device fabrication process to achieve high mobility. Among these, a few noteworthy studies are presented in detail.

Recently, a solution-sharing (blade coating) method has gained popularity for fabricating single-crystal transistors, as it enables the precise control of the molecular alignment at gas/liquid phase interfaces and the fabrication of highly thin single-crystal domains on the substrate, which can then be used as transistors. A new solution-sharing method, called double-blade coating, has also been reported (Fig. 4). It uses two blades: one for the organic semiconductor ink and the other for the water ink. Before depositing the semiconductor ink, the blade applying water is swept across the substrate to form a molecularly flat water surface. When the ink-dissolved C8-BTBT is subsequently applied over it, the number of

Table 1 Recent reports of BTBT-based transistors

Compound[a]	Deposition method of the semiconductor	Mobility ($cm^2 V^{-1} s^{-1}$)	Threshold voltage (V)	On/off ratio	Year	Ref.
1	Sublimation	5.61	−1.56	10^5–10^7	2022	44
	Solution shearing	8.7	−3	10^6–10^7	2024	45
	Spin coating	10.84			2024	46
	Solution shearing	3.53	−0.3	2.6×10^6	2024	47
	Epitaxial growth	1.5			2025	48
	Vacuum deposition	2.45	−16.97	10^8	2024	49
	Solution shearing	0.87	0.1		2025	50
	Vacuum deposition and solution shearing	7.22			2024	51
	Spin casting	0.6 ± 0.3	−4.3 ± 0.6	3.3×10^3	2023	52
	Solution shearing	19.8	−1.26 ± 0.5	$4.3 (\pm 0.5) \times 10^7$	2024	53
	Double-blade coating	15.7	−5	10^7	2024	54
	Solution shearing	2.13	−0.35	4×10^7	2024	55
	Solution shearing	16.1	1.26 ± 0.9	$(7 \pm 3) \times 10^7$	2024	56
	Drop casting	18.6	−0.11	6×10^6	2022	57
	Thermal spin-coating	3.73	−15		2024	58
	Vacuum deposition	6.74	−5		2024	59
	Drop casting	3.59	16.5	9.6×10^6	2022	60
	Solution shearing	6.7			2024	61
2	Solution shearing	9.0 ± 1.5	−20	10^7	2024	62
3	Liquid–liquid interface	2.07	−13.4	7.1×10^6	2022	63
4	Vacuum deposition	3.5×10^{-5}		10^4	2022	64
5	Physical vapor transport	5.4	−40		2024	65
6	Vacuum deposition	6.0×10^{-4}	−54	1.5×10^4	2024	66
7	Spin casting	0.34 (hole) 0.11 (electron)			2023	67
	High-speed solution shearing	4.8 ± 0.35	0.38 ± 0.23		2024	68
8	Dip coating	1.7×10^{-2}	−16 ± 3	10–10^6	2022	69
9	Solution shearing	1.4 ± 0.45	−32 ± 1.4		2023	70
10	Vacuum deposition	1.28 ± 0.02	−3.1 ± 0.7	10^5	2021	71
11	Physical vapor transport	1.35	−14		2024	72
12	Vacuum deposition	0.89			2021	73
13	Spin casting or drop casting	7.5 ± 1.5	2 to −6		2022	74
14	Dipping method	4.7×10^{-1}	−21 to −18	10^5–10^6	2022	75
15	Spin casting	0.26	−23	1.5×10^8	2022	76
16	Continuous wave infrared laser evaporation	1.0×10^{-3}	−22.9		2024	77
17	Continuous wave infrared laser evaporation	2.1×10^{-2}	−9.7		2023	78
18	Vacuum deposition	2.86	−1.2 and −22.2	1.5×10^6	2024	79
	Vacuum deposition	0.2059 ± 0.0251	−8 ± 2.2	$3.5 \times 10^4 \pm 8.7 \times 10^3$	2023	80
19	Vacuum deposition	2.5 to 5			2024	81
20	Vacuum deposition	2.6	−0.07	10^7	2022	82
21	Solution shearing	< 10	−20		2024	83

[a] These numbers correspond to the numbers shown in Fig. 3.

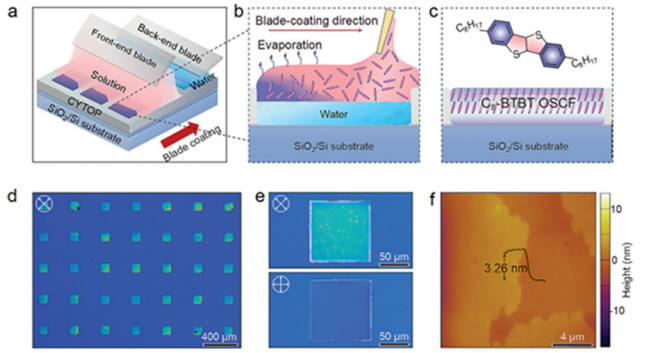

Fig. 4 a) Schematic of the patterning process of C8-BTBT single-crystalline films (OSCFs) based on the technique of double-blade coating. b) An enlarged square wetting area, taken from (a). During the coating process, a small amount of water is dragged into the square wetting area using the back-end blade, and then the front-end blade coats the mixed solution to overprint on the confined water surface. c) The resulting solid C8-BTBT OSCFs. d) Cross-polarized optical microscopy (CPOM) image of C8-BTBT film arrays. e) Magnified CPOM images of a C8-BTBT OSCF at 45° (upper) and 0° (lower) polarization angles, respectively. f) Atomic force microscopy (AFM) image of the C8-BTBT OSCFs. Reprinted with permission from ref. 54. Copyright 2023, WILEY.

crystal nuclei produced in the initial stages of crystallisation is significantly reduced. This approach promotes the formation of large single-crystal films by stimulating crystal growth, enabling the production of single-crystal films of C8-BTBT at an extremely high yield of 62.5%. Transistors using these single crystals show an excellent maximum mobility of up to 15.7 $cm^2 V^{-1} s^{-1}$ and an average of 11.5 $cm^2 V^{-1} s^{-1}$, which is 12.5 times higher than the mobility of reference samples fabricated *via* conventional single-blade coating.[54] Thus, the double-blade coating technique is expected to be widely used in the future.

Doping with acceptor molecules is often used to increase the hole-carrier density in C8-BTBT layers. Typical doping involves the addition of dopants to a fabricated semiconductor layer. Fig. 5 shows a newly reported method, wherein doping is performed simultaneously with semiconductor layer fabrication. Doped single crystals are produced by the conventional blade-coating method using a mixed ink in which 1,3,4,5,7,8-hexafluoro-tetracyanonaphthoquinodimethane (F6-TCNNQ) is dissolved at approximately 0.5 wt% as a dopant in the ink with C8-BTBT as the semiconductor layer. This approach eliminates

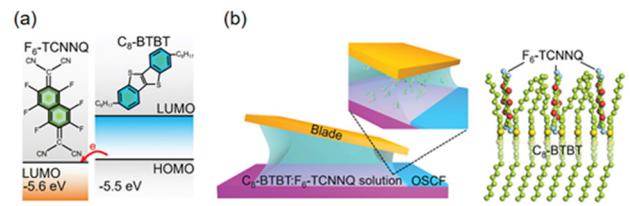

Fig. 5 (a) Chemical structures of C8-BTBT and F6-TCNNQ and schematic of charge transfer between C8-BTBT and F6-TCNNQ. (b) Schematic of solution deposition for anion-doped C8-BTBT thin films. Right: Distribution of F6-TCNNQ anions within the C8-BTBT thin film. Reprinted with permission from ref. 53. Copyright 2024, WILEY.

the traditional problems of dopant diffusion, aggregation, and partial charge transfer only on the surface. Moreover, it enables effective doping into organic single-crystal films without disturbing the molecular arrangement of the semiconductors, thereby improving the OFET performance. Transistors fabricated using this technique exhibit an average mobility of 8.07 $cm^2 V^{-1} s^{-1}$ and a maximum of 19.8 $cm^2 V^{-1} s^{-1}$. These devices are also characterised by their ability to operate at low voltages.[53]

This review presents novel semiconductor materials containing BTBT moieties other than C8-BTBT. In particular, for benzothieno[6,5-*b*]-/benzothieno[5,6-*b*]-benzothieno[3,2-*b*]thiophene (BTBTT) derivatives, the orientation of the condensed thiophene ring significantly influences the molecular arrangement in the crystal, resulting in differences in the characteristics of single-crystal transistors (Fig. 6). The critical parameters for realising a bilayer herringbone (b-HB) structure with excellent crystallinity, favourable for enhanced mobility, have been identified and discussed in detail through a comparative analysis of experimental crystal structures and a hypothetical crystal structure replicated through calculations.[62]

The standard molecular design involves the introduction of a long alkyl group at positions 2 and 7 of the BTBT core; however, 2,7-bis(2(2-methoxyethoxy)ethoxy)benzo[*b*]benzo[4,5]thieno[2,3-*d*]thiophene (OEG-BTBT) has been reported (Fig. 7). This compound has a hydrophilic side chain and an oligoethylene glycol (OEG) group with ionic conductivity, high polarity, and flexibility. The crystal structure of OEG-BTBT is similar to that of other 2,7-substituted BTBT derivatives, with the BTBT core forming a herringbone arrangement. The characteristic is that the OEG chain forms

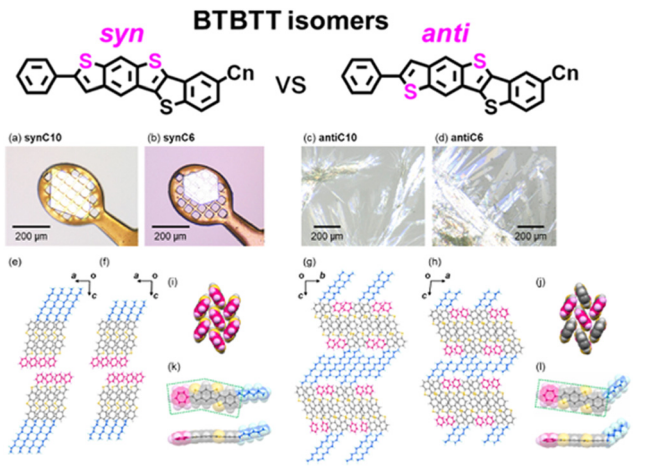

Fig. 6 Optical images of the single crystals of (a) synC10 and (b) synC6 fixed on mesh-type LithoLoops and the crystalline solids of (c) antiC10 and (d) antiC6. Experimental crystal structures projected along the intralayer direction for (e) synC10, (f) synC6, (g) antiC10, and (h) antiC6. Herringbone packings of (i) synC6 and (j) antiC6 (the hexyl chains are omitted for clarity). Top and front views of one molecule of (k) synC6 and (l) antiC6 in the crystals. Green broken frame: approximate molecular shapes of the rigid π-conjugated skeleton composed of the phenyl ring and the BTBTT π-core. Reprinted with permission from ref. 62. Copyright 2024, American Chemical Society.

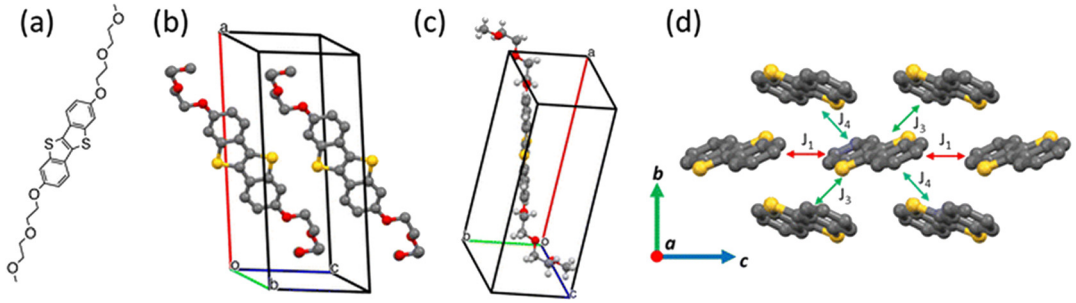

Fig. 7 a) Molecular structure of OEG-BTBT. (b) Molecular packing and (c) conformation of OEG-BTBT in the crystallographic unit cell. (d) Notation of the transfer integrals between the highest occupied molecular orbitals (HOMOs) of neighbouring BTBT units within the herringbone arrangement. The side chains of OEG-BTBT were removed for clarity. Reprinted with permission from ref. 66. Copyright 2024, The Royal Society of Chemistry.

an angled conformation, which is different from that observed for the usual alkyl groups because of the interaction between hydrogen and oxygen atoms of the neighbouring molecules. The values of the intermolecular transfer integrals within the herringbone layer are approximately three times lower than those of similar alkyl-substituted BTBT derivatives. This may be because the angled conformation of the OEG group does not allow sufficient fastener effects to influence the BTBT core. The performances of transistors fabricated by vacuum deposition are lower than those of alkyl-substituted BTBT derivatives. The effect of the voltage-bias stress is particularly noticeable when operating at high gate voltages. These effects are associated with the hydrophilic nature of the OEG side chains, which may increase the concentration of residual water molecules in OEG-BTBT films. The resulting affinity for water, combined with the high ionisation energy of OEG-BTBT, promotes hole trapping in the conducting channel region at the semiconductor/insulator interface. This study indicated that in addition to the stable region of water at the energy level, the chemical properties of the molecule increased the carrier traps derived from water.[66]

Fig. 8 shows an alkylamide-substituted BTBT derivative, BTBT-NHCOC14H29, which achieves transistor properties and ferroelectricity. Dipole moments due to the amide and carbonyl groups were present and ferroelectric hysteresis was observed in the liquid crystal phase (SME phase). Thermal annealing at 443 K changed the structure from a monolayer to a highly crystalline bilayer, with a hole mobility of 1.0×10^{-3} cm^2 V^{-1} s^{-1}. The compound exhibited switching with and without transistor properties after the field poling and thermal annealing cycles. This example demonstrates the effects of the ferroelectric field response on modulating molecular orientation and consequently, the conduction properties of organic transistors.[77]

Organic semiconductors with a herringbone arrangement exhibit high layer crystallinity, which is particularly prominent in bilayer herringbone arrangements. Molecules in which phenyl and alkyl groups are asymmetrically introduced at the 2 and 7 positions of the BTBT skeleton, respectively, are prone to b-HB formation. However, the key factors governing the formation of b-HB arrangements remain unclear. In this regard, a systematic study has been conducted on BTBT derivatives, yielding important findings regarding their b-LHB expression (Fig. 9). In a series of high-layer crystalline organic semiconductors comprising pTol-BTBT-Cn, the solid-state polarity based on the molecular arrangement was reported to be controlled by the odd–even nature of the alkyl groups. The interactions between the tolyl and end methyl groups of the alkyl groups have been carefully evaluated *via* molecular orbital calculations using these crystal structures. The inclination of the terminal methyl group differs depending on the odd–even nature of the alkyl group, altering the aforementioned interactions. Consequently, the molecular arrangement that stabilises the entire crystal structure also changes.[83]

4 Use of BTBT derivatives for other devices

BTBT derivatives have been used not only for the above-mentioned active layers in OFETs but also for other devices. For example, a series of donor–acceptor organic dyes

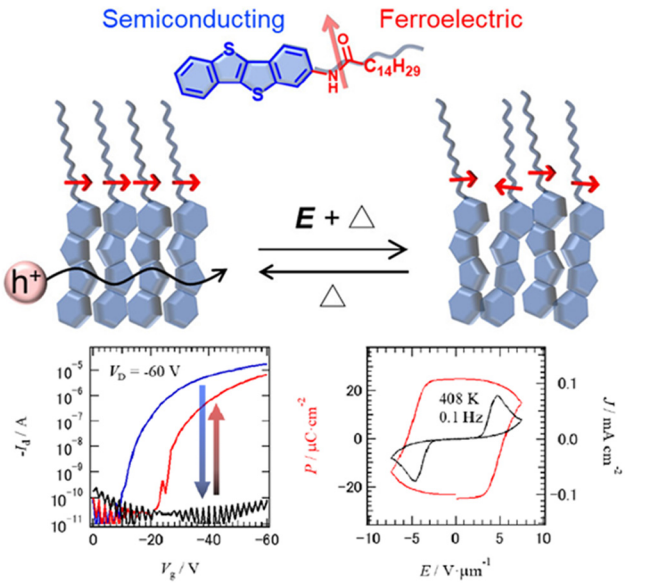

Fig. 8 Molecular structure of BTBT-NHCOC14H29, switching of transfer properties, and ferroelectric behavior. Reprinted with permission from ref. 77. Copyright 2024, American Chemical Society.

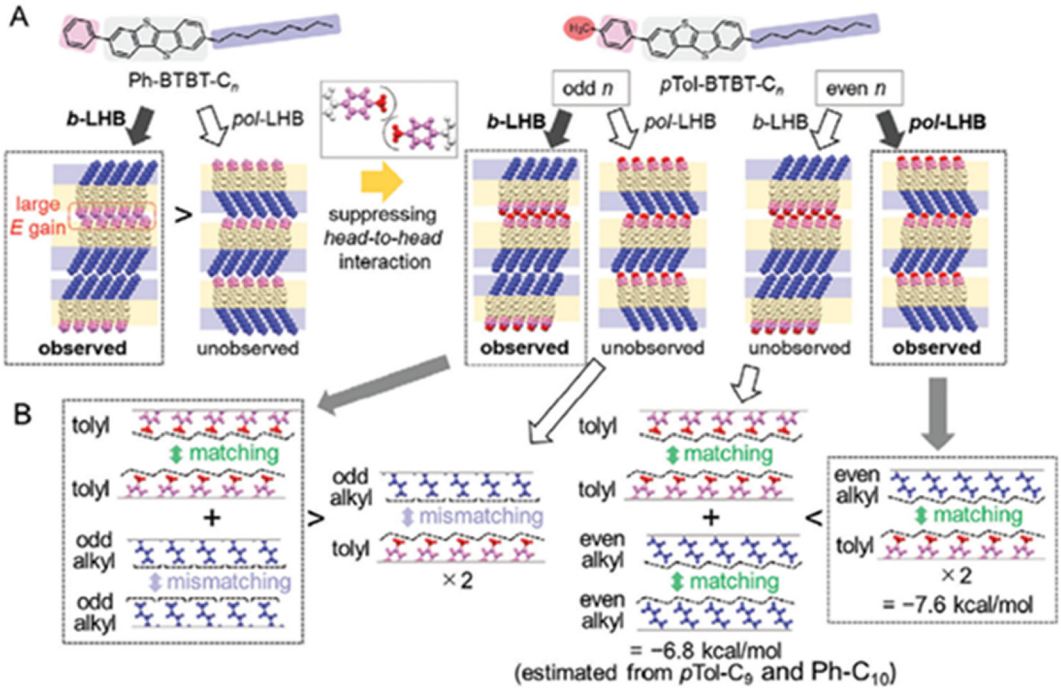

Fig. 9 Schematics of the layer-by-layer stacking combinations. A) Schematics of Ph-BTBT-Cn (left) and pTol-BTBT-Cn (right). The orange and blue areas show BTBT-core layers and alkyl chain layers, respectively. B) Schematics of the affinities in the layer surface for tolyl groups, odd-*n* alkyl chains, and even-*n* alkyl chains. The black dashed lines schematically show the boundary of the space-filling surface. Reprinted with permission from ref. 83. Copyright 2024, WILEY.

containing the BTBT skeleton as the π-bridging moiety were designed for dye sensitised solar cells (DSSCs) (Fig. 10(a)).[84] While the acceptor moiety was fixed with a cyanoacrylic group, the donor moiety was varied from fluorenylthiophene (molar extinction coefficients (ε) > 14 000) through bisfluorenylamine (ε > 42 000) to bisfluorenylphenothiazin (ε > 69 000), achieving considerable enhancement of absorptivity. These organic dye-based DSCCs exhibited good photovoltaic performances,

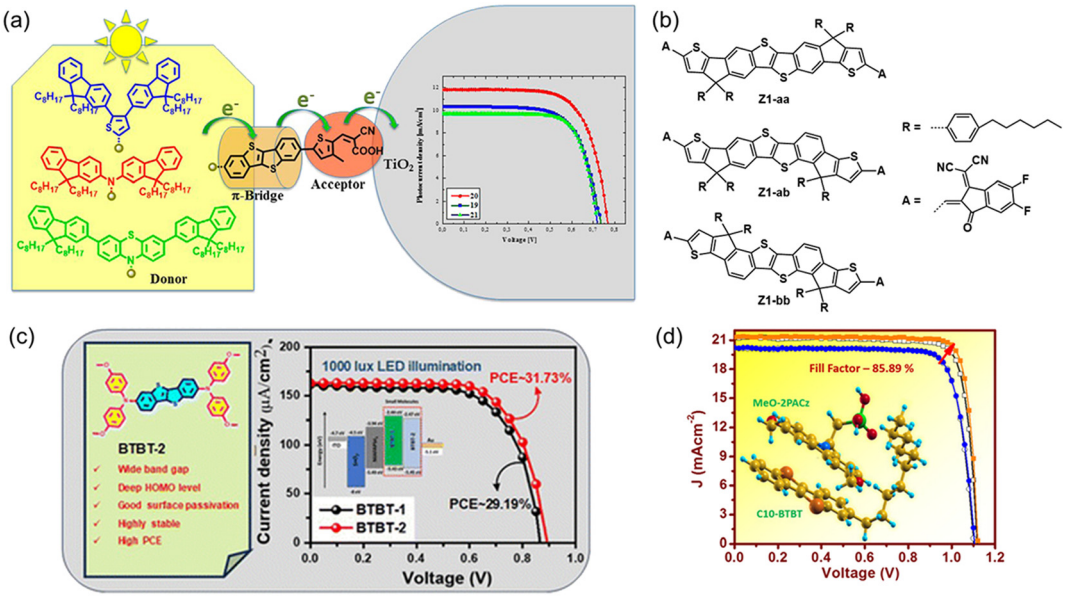

Fig. 10 (a) Donor–acceptor organic dyes containing the BTBT skeleton as the π-bridging moiety applied to DSCCs. Reprinted with permission from ref. 84. Copyright 2016, American Chemical Society. (b) BTBT-based octacyclic molecules used as non-fullerene acceptors in organic solar cells. (c) BTBT-based hole-transporting materials used in PPVs. Reprinted with permission from ref. 86. Copyright 2024, The Royal Society of Chemistry. (d) Use of a BTBT derivative as an interlayer between a SAM-based hole-transporting layer and an active layer in PPVs. Reprinted with permission from ref. 87. Copyright 2023, Wiley-VCH.

highlighting the suitable electron-transport properties of the BTBT π-bridge.

Another example of BTBT derivatives applied to photovoltaic devices is BTBT-based octacyclic molecules used as non-fullerene acceptors in organic solar cells (OSCs) (Fig. 10(b)).[85] Although BTBT derivatives usually serve as electron donors, covalent attachment of the 2-(5,6 difluoro-2-methylene-3-oxo-2,3-dihydro-1*H*-inden-1-ylidene) malononitrile moieties at both ends transforms the octacyclic BTBT precursors to electron donors. The OSC devices based on Z1-bb blended with an electron donor exhibited a higher power conversion efficiency (PCE) of 12.66% than the Z1-ab-based (9.60%) and Z1-aa-based (4.56%) devices. This example demonstrates that the isomerisation of highly fused-ring acceptors can modulate photovoltaic performance.

BTBT derivatives have also been used as hole-transporting materials in perovskite photovoltaics (PPVs). A BTBT derivative with one and two 4,4′-dimethoxydiphenylamino groups exhibited a power conversion efficiency (PCE) of 29.19% and 31.73%, respectively, under the illumination of a 1000 lux LED lamp for indoor PPV devices (Fig. 10(c)).[86] These PCE values are higher than that of a PPV device containing 2,2′,7,7′-tetrakis[*N*,*N*-di(4-methoxyphenyl)amino]-9,9′-spirobifluorene, a leading hole-transporting molecular material (28.87%). Moreover, the hydrophobic nature of the BTBT derivatives is advantageous for improving device stability. In another PPV device, 2-decyl[1]benzothieno[3,2-*b*][1]benzothiophene was inserted between a self-assembled monolayer (SAM)-based hole-transporting layer and a perovskite active layer (Fig. 10(d)).[87] DFT calculations suggested that the monoalylated BTBT derivative could interact with the carbazole-based SAM *via* π–π stacking. The interlayer of the monoalylated BTBT derivative enhanced the extraction of charges from the perovskite active layer to the SAM-based hole-transporting layer, increasing the PCE from 18.04% to 20.50%. In the context of perovskite research, a BTBT derivative with a propylammonium chain was used to prepare hybrid organic–inorganic perovskites.[88]

BTBT-based charge-transfer complexes have been demonstrated to be useful thermoelectric materials. Thermoelectric composites were prepared by combining charge-transfer complexes composed of C8-BTBT and 2,3,5,6-tetrafluoro-7,7,8,8-tetracyano-quinodimethane (F4TCNQ) with single-walled carbon nanotubes; the LUMO level of the charge-transfer complex was comparable with the Fermi level of the carbon nanotubes. This promoted electron transport in the n-type composition film.[89] The composite had low defects with moderate carrier concentrations, affording a good n-type power factor of 105.1 μW m^{-1} K^{-2}. Regarding BTBT-based thermoelectric functions, the thermoelectric properties of SAM composed of thiolated and alkylated BTBT derivatives on Au were investigated.[90] For the C8-BTBT molecular junctions, the photonic thermal transport was efficiently reduced by the alkyl chains, generating a low value of 8.8 pW K^{-1}. A high expected Seebeck coefficient of 245 μV K^{-1} coincided with a large reduction of the electron conductance.

5 Fabrication of metal complexes containing BTBT skeletons as π-extended ligands

Although BTBT derivatives have long been investigated as OFET materials, chemical modifications of the BTBT skeleton have recently been conducted to explore new molecular functions. One approach is to introduce BTBT skeletons into metal complex structures as π-extended ligands to synergise the BTBT- and metal complex-derived functions. The first examples of metal complexes containing BTBT skeletons in ligands were π-extended catecholato Pt(II) and Pd(II) complexes synthesized with a 2,3-dihydroxy-substituted BTBT derivative (Fig. 11(a)).[91] The Pt(II) and Pd(II) complexes exhibited intramolecular charge transfer (ICT) transition bands from the ancillary bipyridyl to the π-extended catecholato ligand at 546 and 530 nm in CH_2Cl_2, respectively, showing purple colours. Moreover, in their one-electron-oxidised state, these complexes exhibited π–π* ICT transition bands within the π-extended catecholato ligand, producing a green colour. These findings provide insights into the optical properties of small-molecule organic semiconducting units.

A π-extended catecholato Pt(II) complex with auxiliary dimethyl sulfoxide (DMSO) ligands was used as a constituent molecule for SAMs (Fig. 11(b)).[92] Ligand exchange from the DMSO ligands to the OH groups proceeded at the surface of the SiO_2 gate insulator, affording SAMs derived from the Pt(II) complex containing a BTBT skeleton. X-ray photoelectron spectroscopy and atomic force microscopy revealed that the π-extended catecholato ligand was partially oxidised by aerobic oxidation. Homogeneous thin films of C8-BTBT were deposited on SAMs formed on SiO_2/Si substrates by vacuum thermal evaporation. The C8-BTBT molecules engaged with the SAMs through π–π interactions of the common BTBT skeletons. These unique interfacial structures improved the OFET performance in terms of hole mobility and onset voltage, while the ON/OFF ratio decreased. This example demonstrates the utility of introducing coordination chemistry in solution onto insulator surfaces to fabricate new functional interfaces with organic semiconductors. Notably, ferrocene (Fc)-SAM-based OFETs with C8-BTBT showed pronounced hysteresis in the source–drain current between the forward and backward scans.[93] The Fc-based SAMs served as a charge-trapping layer, which is a key component for constructing nonvolatile OFET memory devices.

Regarding OFETs containing an Fc-based SAM, a covalent conjugate composed of ferrocene and BTBT has been synthesised and characterised (Fig. 11(c)).[94] The Fc–BTBT conjugate adopted a packing motif involving both intermolecular homotypic interactions (Fc⋯Fc and BTBT⋯BTBT) and heterotypic interactions (Fc⋯BTBT). The conjugate displayed a pronouncedly reversible Fe(III)/Fe(II) redox couple, indicating that its redox behaviour was derived from the Fc moiety. The one-electron-oxidised species of the conjugate can be expressed as ferrocenium–

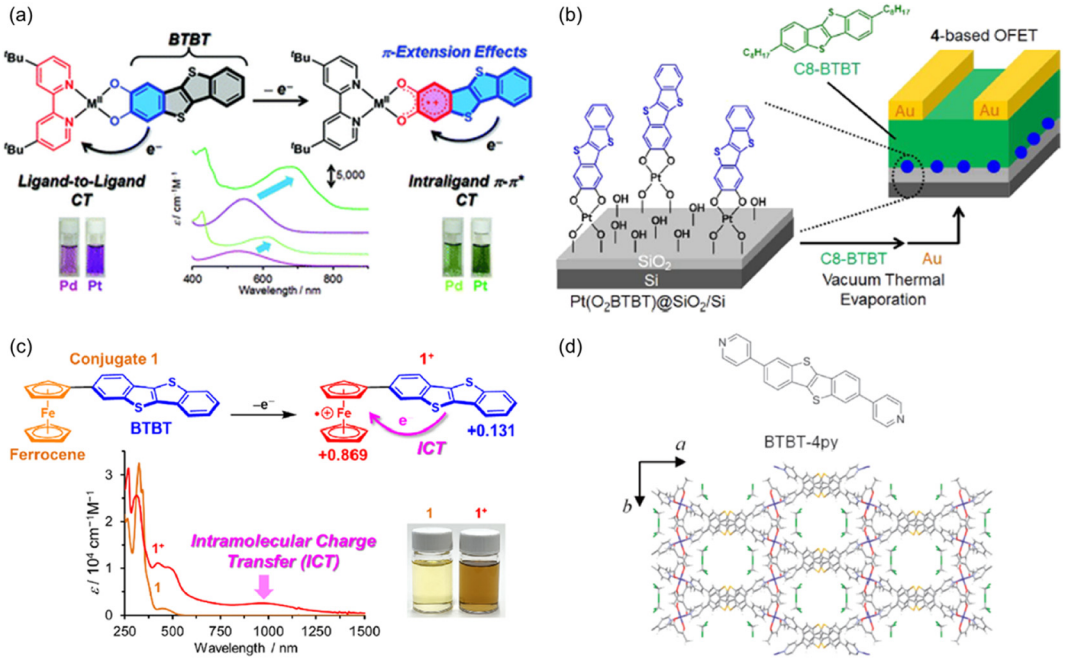

Fig. 11 (a) Charge transfer of π-extended catecholato Pt(II) and Pd(II) complexes in neutral and one-electron-oxidized forms. Reprinted with permission from ref. 91. Copyright 2019, The Royal Society of Chemistry. (b) OFET device inserting a Pt(II) complex-based SAM between SiO_2 and C8-BTBT layers. Reprinted with permission from ref. 92. Copyright 2020, American Chemical Society. (c) ICT from BTBT to ferrocene moieties in a ferrocene–BTBT conjugate in the one-electron-oxidized form. Reprinted with permission from ref. 94. Copyright 2025, American Chemical Society. (d) Crystal structure of linear coordination polymers composed of Co(II) ions and dipyridylated BTBT ligands. Reprinted with permission from ref. 96. Copyright 2019, The Chemical Society of Japan.

BTBT, where the positive charge was primarily located on the Fc moiety. The ferrocenium–BTBT was directly generated by chemical oxidation and exhibited an ICT absorption band from the BTBT to ferrocenium moieties in solution. The stability of ferrocenium–BTBT is advantageous for future applications as an active layer in nonvolatile OFET memory devices.

Recently, crystalline porous framework materials have received considerable attention due to their various applications, including gas storage and separation, catalysis, and sensing. Among the studies on covalent organic frameworks (COFs), one used a covalent triazine framework synthesised from 4,4′-(benzo[*b*]benzo[4,5]thieno[2,3-d]thiophene-2,7-diyl)dibenzonitrile as a metal-free heterogeneous photocatalyst.[95] This COF-based photocatalyst showed visible-light absorptivity based on ICT from π-extended BTBT to triazine moieties. Among the studies on porous coordination polymers, Iguchi *et al.* fabricated linear coordination polymers *via* coordination reactions of [Co(acetylacetylacetonate)2)] and 2,7-bis(4-pyridyl)-[1]benzothieno[3,2-*b*][1]benzothiophene (BTBT–4py) (Fig. 11(d)).[96] The linear coordination polymers stacked at the BTBT moieties alternately in two different directions formed large pores filled by $CHCl_3$ molecules. Desolvation upon heating induced large irreversible structural changes in the coordination polymers, as evidenced by the change in the powder X-ray diffraction (XRD) patterns. This approach to forming pores with π-stacked structures is promising for introducing new functionalities into the active layers of OFETs.

6 Fabrication of BTBT-based luminescent materials

BTBT has not received attention as a luminescent molecular material because it exhibits weak fluorescence from the π–π* transition state in solution. In CH_2Cl_2, BTBT shows a fluorescence band at 342 nm with vibrational structures whose fluorescence quantum yield is 0.034, whereas the fluorescence lifetime is 0.10 ns.[97]

Fluorescence spectral data of BTBT derivatives such as 2,7-dibromo-substituted BTBT[98] and BTBT–peptide conjugates have been presented.[99] π-Extension of BTBT with a thiophene ring substantially improved the fluorescence quantum yield, reaching 0.73.[100]

In the solid state, BTBT showed a fluorescence band at 397 nm with vibrational structures,[97] with a fluorescence quantum yield of 0.013, whereas the fluorescence lifetime was 0.34 ns. Therefore, BTBT is a weak emitter in the solid state; however, C10-BTBT and Ph-BTBT-C10 can be used as active layers in organic light-emitting transistor (OLET) devices, displaying UV and deep blue emissions, respectively, and achieving high hole transfer mobilities.[101] Recently, C12-BTBT-based OLET devices have been fabricated exhibiting electrofluorochromic behaviour, where the fluorescence properties were modulated by regulating space charges in the dielectric layer.[102] These OLET performances indicate that BTBT derivatives have the potential to function as hole-transporters and emitters. However, the weak fluorescence

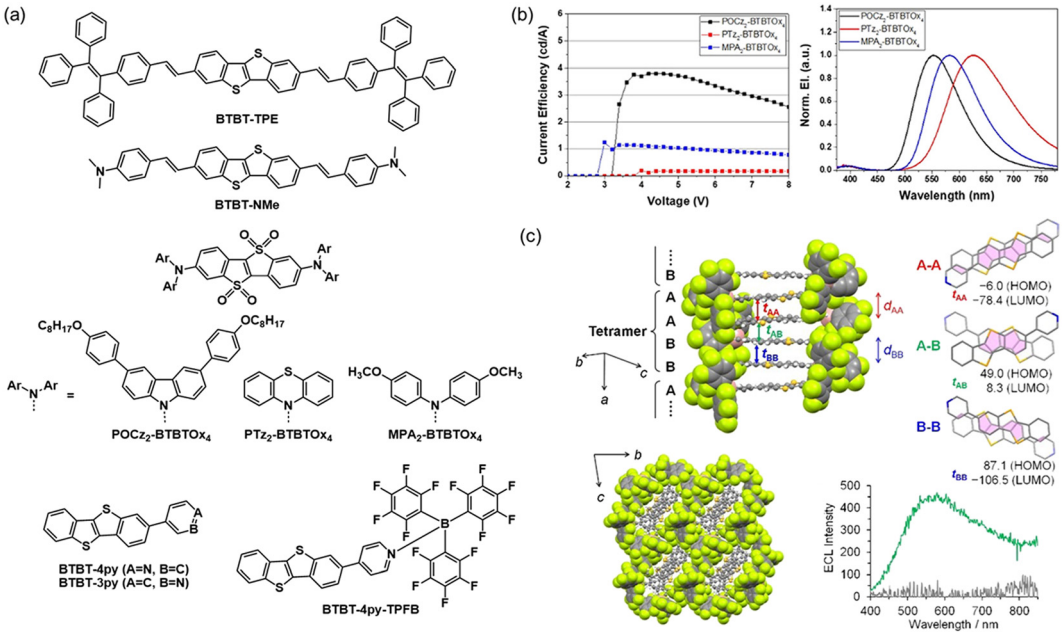

Fig. 12 (a) Structures of BTBT-based luminescent molecules. (b) The current efficiency and electroluminescence spectra of OLEDs using $POCz_2$–$BTBTOx_4$, PTz_2–$BTBTOx_4$ and MPA_2–$BTBTOx_4$ as emitting layers. Reprinted with permission from ref. 104. Copyright 2025, The Royal Society of Chemistry. (c) Crystal structures of BTBT–4py–TPFB with transfer integral values and electrochemiluminescence from the crystalline film of BTBT–4py–TPFB with a co-reactant in PBS aqueous solutions. Reprinted with permission from ref. 97. Copyright 2023, Wiley-VCH.

intensity of BTBT derivatives must be fundamentally improved for applications in light-emitting devices.

Aggregation-induced emission (AIE) is a well-known phenomenon often used to develop organic solid-state luminescent materials. The tetraphenylethylene (TPE) skeleton is one of the most widely investigated AIE motifs. Singh *et al.* covalently connected two TPE moieties on both sides of BTBT *via* ethylene linkers to afford a BTBT-based dye, BTBT–TPE (Fig. 12(a)).[103] BTBT–TPE showed AIE behaviour with a fluorescence quantum yield of 0.283 in a mixed solvent of water and tetrahydrofuran (THF); this value is 8.1 times higher than that for THF. In contrast, its dimethylamine counterpart (BTBT–NMe) exhibited aggregation-induced quenching behaviour. Notably, these BTBT-based dyes exhibited mechanofluorochromic properties; their fluorescence maxima were blue-shifted upon grinding and red-shifted upon fuming with organic solvents.

Thermally activated delayed fluorescence (TADF) is another powerful phenomenon that has recently attracted considerable attention. TADF methods can be used for fabricating high-performance organic light-emitting diodes (OLEDs). Maggiore *et al.* used BTBT–tetraoxide $BTBTOx_4$ as an electron acceptor and covalently connected two electron donors at both ends to develop three D–A–D conjugates POCz2–$BTBTOx_4$, PTz2–$BTBTOx_4$, and MPA2–$BTBTOx_4$ (Fig. 12(b)).[104] Detailed photophysical investigations revealed that these BTBT-based emitters possessed TADF properties. Specifically, $POCz_2$–$BTBTOx_4$ and MPA_2–$BTBTOx_4$ exhibited high photoluminescence quantum yields of 0.688 and 0.596, respectively, in cyclohexane. Although MPA_2–$BTBTOx_4$ self-quenched on neat films, $POCz_2$–$BTBTOx_4$ maintained a relatively high quantum yield of 0.22. OLED devices containing neat films of these BTBT-based emitters exhibited electroluminescence, with emission maxima trends corresponding to those in the photoluminescence spectra (Fig. 12(b)). Current efficiency was significantly higher for the $POCz_2$–$BTBTOx_4$-based device than for the PTz_2–$BTBTOx_4$- and MPA_2–$BTBTOx_4$-based devices because the bulky structure of $POCz_2$–$BTBTOx_4$ inhibited self-quenching upon device operation.

Other examples of BTBT-based D–A conjugates are pyridylated BTBT derivatives with a pyridyl moiety as an electron acceptor (Fig. 12(a)).[97] BTBT–4py and BTBT–3py showed fluorescence from the ICT states of BTBT to pyridyl moieties with fluorescence quantum yields of 0.122 and 0.212, respectively, in CH_2Cl_2. BTBT–3py was used as a ligand for a cyclometalated Pt(II) complex.[105] The fluorescence of the Pt complex was quenched in solution, accompanied by intersystem crossing enhanced by heavy-atom effects. The resulting triplet ICT excited state was captured by femtosecond transient absorption spectroscopy. BTBT–3py was also used as a ligand for a dinuclear Cu(I) complex.[106] The iodo-bridged dicopper complex had a deformed Cu_2I_2 core and contained solvent molecules that filled the channels of the crystals. The solid-state photoluminescence of the dicopper complex was unusually red-shifted because of the large structural relaxation and intermolecular electronic coupling between the BTBT moieties. The pyridylated BTBT derivatives were complexed with the bulky Lewis acid tris(pentafluorophenyl)borane (TPFB),[97] and the resulting BTBT–4py–TPFB and BTBT–3py–TPFB complexes exhibited fluorescence quantum yields of 0.688 and 0.326, respectively, in CH_2Cl_2. The improved fluorescence resulted from the inhibition of nonradiative decay by the restricted molecular motion of the bulky TPFB moiety. Moreover, the TPFB moieties stabilised the electrogenerated radical cations

and anions, with charges distributed on the pyridylated BTBT moieties. Accordingly, BTBT–4py–TPFB exhibited a 156-fold increase in electrochemiluminescence (ECL) compared to BTBT–4py, a phenomenon termed Lewis-pairing-induced ECL enhancement. Furthermore, single-crystal XRD analysis of BTBT–4py–TPFB revealed that the pyridylation of BTBT, followed by complexation with TPFB, transformed the molecular packing from herringbone to one-dimensional columnar structures (Fig. 12(c)). BTBT–4py–TPFB exhibited ECL from a crystalline film on an electrode with $K_2S_2O_8$ in PBS aqueous solutions. The crystalline film ECL was red-shifted compared to the ECL solution, reflecting singlet exciton delocalisation within the π-stacked column.

7 Conclusion

This review highlighted studies on functional materials based on the BTBT skeleton, demonstrating their potential as excellent organic transistor materials. The molecular kink based on the central thienothiophene moiety of the BTBT skeleton results in a deeper HOMO level than that of similar aromatic hydrocarbons, leading to the stable operation of p-type transistors in air. The benzene ring fused to thienothiophene is localised to the HOMO largely over a sulfur atom, which is important for forming effective intermolecular transfer integrals. The chemical properties of this molecular unit significantly enhance the hole-transport properties of transistors by forming molecular assemblies with 2D electronic structures, such as a herringbone arrangement. Recently, materials that impart composite functions in addition to the switching properties of transistors have been developed. Furthermore, with the advancement of single-crystal device fabrication processes, hole mobilities realised by BTBT derivatives have frequently reached the order of 10 $cm^2 V^{-1} s^{-1}$. Recent advances in the use of BTBT derivatives have significantly expanded their application beyond OFETs. These derivatives have demonstrated utility in OSCs and PPVs, primarily owing to their excellent charge transport properties derived from their effective intermolecular transfer integrals. Furthermore, BTBT-based charge-transfer complexes and SAMs have been explored for thermoelectric and interface-engineering applications. The incorporation of BTBT units into metal complexes results in synergistic optical and redox properties. In the field of luminescent materials, although pristine BTBT exhibits weak fluorescence, structural modifications such as π-extension, donor–acceptor conjugation, and incorporation into AIE or TADF systems have markedly enhanced emission properties. Notably, BTBT-based emitters have achieved promising performance in OLEDs and OLETs, with the potential for dual charge transport and light-emission functionalities. Lewis complexation of pyridylated BTBT with bulky Lewis acids has also shown electrochemiluminescence enhancement and structural transformations in the solid state. Overall, these developments highlight the versatility of the BTBT scaffolds for next-generation organic electronic and photonic devices. The utilisation of coordination chemistry will further advance the development of functional materials for light-emitting devices, nonvolatile memory devices, and hybrid device architectures.

Author contributions

T. K. and K. T. have equal contributions to this paper. Sections 1–3 were mainly written by T. K., and 4–6 by K. T., respectively. Table 1 was prepared by T. I., H. S., Y. K., H. T., M. S., and T. K. H. K. and M. Y. partly contributed to the molecular orbital calculations and discussion of the energy levels of water in section 2. All authors discussed each section and commented on the manuscript.

Conflicts of interest

There are no conflicts to declare.

Data availability

This is a highlight article, without new data input herein. All data can be sourced from the referenced articles. The DFT data that support the findings of this study are openly available upon request from the corresponding author.

Acknowledgements

This work was partly supported by the JSPS KAKENHI Grant Number 23K04882 and the Research Funds for General Research Institute.

Notes and references

1 K. Liu, B. Ouyang, X. Guo, Y. Guo and Y. Liu, *npj Flexible Electron.*, 2022, **6**, 1.
2 J. Song, H. Liu, Z. Zhao, P. Lin and F. Yan, *Adv. Mater.*, 2024, **36**, 2300034.
3 C. Wang, H. Dong, W. Hu, Y. Liu and D. Zhu, *Chem. Rev.*, 2012, **112**, 2208.
4 T. Higashino and T. Mori, *Phys. Chem. Chem. Phys.*, 2022, **24**, 9770.
5 B. Kumar, B. K. Kaushik and Y. S. Negi, *Polym. Rev.*, 2014, **54**, 33.
6 T. Hasegawa and S. Inoue, *JSAP Rev.*, 2022, 220206.
7 H. M. Yamamoto, *Bull. Chem. Soc. Jpn.*, 2021, **94**, 2505.
8 T. Mori, *CrystEngComm*, 2025, **27**, 889–902.
9 T. Mori, *CrystEngComm*, 2023, **25**, 6266–6278.
10 K. Takimiya, K. Bulgarevich and K. Kawabata, *Acc. Chem. Res.*, 2024, **57**, 884–894.
11 C. Reese, M. Roberts, M.-M. Ling and Z. Bao, *Mater. Today*, 2004, **7**, 20.
12 K. Takimiya, H. Ebata, K. Sakamoto, T. Izawa, T. Otsubo and Y. Kunugi, *J. Am. Chem. Soc.*, 2006, **128**, 12604–12605.
13 K. Takimiya, Y. Kunugi, Y. Konda, H. Ebata, Y. Toyoshima and T. Otsubo, *J. Am. Chem. Soc.*, 2006, **128**, 3044–3050.
14 H. Ebata, T. Izawa, E. Miyazaki, K. Takimiya, M. Ikeda, H. Kuwabara and T. Yui, *J. Am. Chem. Soc.*, 2007, **129**, 15732–15733.

15 K. Takimiya, S. Shinamura, I. Osaka and E. Miyazaki, *Adv. Mater.*, 2011, **23**, 4347.
16 K. Takimiya, I. Osaka, T. Mori and M. Nakano, *Acc. Chem. Res.*, 2014, **47**(5), 1493–1502.
17 P. Xie, T. Liu, J. Sun and J. Yang, *Adv. Funct. Mater.*, 2022, **32**, 2200843.
18 H. Meng, L. Zheng, A. J. Lovinger, B.-C. Wand, P. G. V. Patten and Z. Bao, *Chem. Mater.*, 2003, **15**, 1778.
19 N. M. Marković, H. A. Gasteiger and P. N. Ross Jr, *J. Phys. Chem.*, 1995, **99**, 3411–3415.
20 M. Kanno, Y. Bando, T. Shirahata, J. Inoue, H. Wada and T. Mori, *J. Mater. Chem.*, 2009, **19**, 6548–6555.
21 T. Yoshino, K. Shibata, H. Wada, Y. Bando, K. Ishikawa, H. Takezoe and T. Mori, *Chem. Lett.*, 2009, **38**, 200–201.
22 Y. Takahashi, T. Hasegawa, S. Horiuchi, R. Kumai, Y. Tokura and G. Saito, *Chem. Mater.*, 2007, **19**, 6382.
23 T. Kakinuma, H. Kojima, T. Kawamoto and T. Mori, *J. Mater. Chem. C*, 2013, **1**, 2900–2905.
24 H. Okamoto, S. Hamao, H. Goto, Y. Sakai, M. Izumi, S. Gohda, Y. Kubozono and R. Eguchi, *Sci. Rep.*, 2014, **4**, 5048.
25 H. Okamoto, N. Kawasaki, Y. Kaji, Y. Kubozono, A. Fujiwara and M. Yamaji, *J. Am. Chem. Soc.*, 2008, **130**, 10470–10471.
26 Y. Kubozono, X. He, S. Hamao, K. Teranishi, H. Goto, R. Eguchi, T. Kambe, S. Gohda and Y. Nishihara, *Eur. J. Inorg. Chem.*, 2014, 3806–3819.
27 J. Poater, R. Visser, M. Sola and F. M. Bickelhaupt, *J. Org. Chem.*, 2007, **72**, 1134.
28 E. M. Engler and V. V. Patel, *J. Am. Chem. Soc.*, 1974, **96**, 7376.
29 K. Bechgaard, D. O. Cowan and A. N. Bloch, *J. Chem. Soc., Chem. Commun.*, 1974, 937.
30 D. Jérome, A. Mazaud and M. Ribault, *J. Phys., Lett.*, 1980, **41**, L95.
31 G. Saito, T. Enoki, K. Toriumi and H. Inokuchi, *Solid State Commun.*, 1982, **42**, 557.
32 H. Kojima and T. Mori, *Bull. Chem. Soc. Jpn.*, 2011, **84**, 1049–1056.
33 L. Zhang, N. S. Colella, B. P. Cherniawski, S. C. B. Mannsfeld and A.s L. Briseno, *ACS Appl. Mater. Interfaces*, 2014, **6**, 5327–5343.
34 C. Zhang and X. Zhu, *Adv. Funct. Mater.*, 2020, **30**, 2000765.
35 A. R. Murphy and J. M. J. Fréchet, *Chem. Rev.*, 2007, **107**, 1066–1096.
36 C. Mitsui, T. Okamoto, M. Yamagishi, J. Tsurumi, K. Yoshimoto, K. Nakahara, J. Soeda, Y. Hirose, H. Sato, A. Yamano, T. Uemura and J. Takeya, *Adv. Mater.*, 2014, **26**, 4546–4551.
37 T. Fujino, R. Kameyama, K. Onozuka, K. Matsuo, S. Dekura, T. Miyamoto, Z. Guo, H. Okamoto, T. Nakamura, K. Yoshimi, S. Kitou, T. Arima, H. Sato, K. Yamamoto, A. Takahashi, H. Sawa, Y. Nakamura and H. Mori, *Nat. Commun.*, 2024, **15**, 3028.
38 J. Takeya, M. Yamagishi, Y. Tominari, R. Hirahara, Y. Nakazawa, T. Nishikawa, T. Kawase, T. Shimoda and S. Ogawa, *Appl. Phys. Lett.*, 2007, **90**, 102120.
39 V. Podzorov, E. Menard, A. Borissov, V. Kiryukhin, J. A. Rogers and M. E. Gershenson, *Phys. Rev. Lett.*, 2004, **93**, 086602.
40 K. Bulgarevich and K. Takimiya, *CrystEngComm*, 2025, **27**, 4776.
41 K. Takimiya, M. Nakano, H. Sugino and I. Osaka, *Synth. Met.*, 2016, **217**, 68–78.
42 T. Izawa, E. Miyazaki and K. Takimiya, *Chem. Mater.*, 2009, **21**, 903–912.
43 D. Zheng, Y. Guo, M. Zhang, X. Feng, L. Zhu, L. Qiu, X. Jin and G. Zhao, *J. Comput. Chem.*, 2020, **41**, 976–985.
44 Q. Lin, X. Ye, Q. Guo, X. Zheng, Q. Han, L. Zhang, S. Cui, C. Li, J. Jiang, Y. Liu and X. Tao, *Chem. Mater.*, 2022, **34**, 1030–1040.
45 B. Geng, F. Zhang, C. Huang, L. He, C. Li, S. Duan, X. Ren and W. Hu, *J. Mater. Chem. C*, 2024, **12**, 5012–5018.
46 M. Zhang, M. Du, Y. Tong, X. Wang, J. Sun, S. Guo, X. Zhao, Q. Tang and Y. Liu, *J. Mater. Chem. C*, 2024, **12**, 7732–7740.
47 R. Duan, S. Liu, X. Liu, M. Huang, S. He, H. Liu, W. Liu and C. Zhu, *J. Mater. Chem. C*, 2024, **12**, 6671–6679.
48 P. Keo, T. Yan, J. Wang, X. Zhang, Y. Shi and J. Jie, *RSC Adv.*, 2025, **15**, 9891–9898.
49 C. Yan, Q. Wang, W. Gong, J. Lu, Y. Yin, C. Xiang, D. Xue, Z. Wang, L. Huang and L. Chi, *Chem. Commun.*, 2024, **60**, 10132–10135.
50 J. P. Andrade, A. W. Lashkova, A. Prasoon, F. Talnack, K. Haase, B. Büchner, X. Feng, Y. Vaynzof, M. Hambsch, Y. Krupskaya and S. C. B. Mannsfeld, *Adv. Electron. Mater.*, 2025, **11**, 2400312.
51 T. J. Mun, J. Kim, J. Seong, Y. Jang, W. Lee and H. Seong, *Adv. Electron. Mater.*, 2024, **10**, 2300800.
52 K. Gubanov, M. Johnson, M. Akay, B. C. Wolz, D. Shen, X. Cheng, S. Christiansen and R. H. Fink, *Adv. Electron. Mater.*, 2023, **9**, 2201233.
53 A. Dong, W. Deng, Y. Wang, X. Shi, F. Sheng, Y. Yin, X. Ren, J. Jie and X. Zhang, *Adv. Funct. Mater.*, 2024, **34**, 2404558.
54 Y. Xiao, W. Deng, J. Hong, X. Ren, X. Zhang, J. Shi, F. Sheng, X. Zhang and J. Jie, *Adv. Funct. Mater.*, 2023, **33**, 2213788.
55 S. Duan, X. Zhang, Y. Xi, D. Liu, X. Zhang, C. Li, L. Jiang, L. Li, H. Chen, X. Ren and W. Hu, *Adv. Mater.*, 2024, **36**, 2405030.
56 F. Sheng, W. Deng, X. Ren, X. Liu, X. Meng, J. Shi, S. Grigorian, J. Jie and X. Zhang, *Adv. Mater.*, 2024, **36**, 2401822.
57 B. Fu, F. Yang, L. Sun, Q. Zhao, D. Ji, Y. Sun, X. Zhang and W. Hu, *Adv. Mater.*, 2022, **34**, 2203330.
58 D. Zhang, X. Zheng, C. He, Y. He and H. Meng, *Appl. Phys. Lett.*, 2024, **124**, 123301.
59 Q. Xu, H. Wei, Y. Lin, Z. Yan and W. Wang, *Appl. Phys. Lett.*, 2024, **124**, 143301.
60 T. Hawly, M. Johnson, A. Späth, H. N. Jäkel, M. Wu, E. Spiecker, B. Watts, A. Nefedov and R. H. Fink, *ACS Appl. Mater. Interfaces*, 2022, **14**, 16830–16838.

61 C. Huang, C. Li, B. Geng, X. Ding, J. Zhang, W. Tang, S. Duan, X. Ren and W. Hu, *ACS Appl. Mater. Interfaces*, 2024, **16**, 30228–30238.
62 T. Higashino, S. Inoue, S. Arai, S. Tsuzuki, H. Matsui, R. Kumai, K. Takaba, S. Maki-Yonekura, H. Kurokawa, I. Inoue, K. Tono, K. Yonekura and T. Hasegawa, *Chem. Mater.*, 2024, **36**, 848–859.
63 T. Hawly, M. Johnson, B. Zhao, M. Wu, A. Späth, F. Streller, H. N. Jäkel, M. Halik, E. Spiecker, B. Watts, A. Nefedov and R. H. Fink, *ACS Appl. Electron. Mater.*, 2022, **4**, 5914–5921.
64 M. Talamo, F. Pop, P. Hume, M. Abbas, G. Wantz and N. Avarvari, *J. Mater. Chem. C*, 2022, **10**, 8034–8042.
65 M. Qi, D. Zhang, Y. Zhu, C. Zhao, A. Li, F. Huang, Y. He and H. Meng, *J. Mater. Chem. C*, 2024, **12**, 6578–6587.
66 M. Gicevičius, A. James, L. Reicht, N. McIntosh, A. Greco, L. Fijahi, F. Devaux, M. Torrent, J. Cornil, Y. Geerts, E. Zojer, R. Resel and H. Sirringhaus, *Mater. Adv.*, 2024, **5**, 6285–6294.
67 X. Ji, J. Zheng, T. Lin, L. Liu, H. Wei, C. Chen, J. Xiong, X. Wang, J. Li and F. Yan, *J. Mater. Chem. C*, 2023, **11**, 12583–12589.
68 I. Suzuki, J. Hanna and H. Iino, *Appl. Phys. Express*, 2024, **17**, 051007.
69 M. S. Polinskaya, A. A. Trul, O. V. Borshchev, M. S. Skorotetcky, V. P. Gaidarzhi, S. K. Toirov, D. S. Anisimov, A. V. Bakirov, S. N. Chvalun, E. V. Agina and S. A. Ponomarenko, *J. Mater. Chem. C*, 2023, **11**, 1937–1948.
70 P. Pandey, L. Fijahi, N. McIntosh, N. Turetta, M. Bardini, S. Giannini, C. Ruzié, G. Schweicher, D. Beljonne, J. Cornil, P. Samorì, M. M. Torrent, Y. H. Geerts, E. Modena and L. Maini, *J. Mater. Chem. C*, 2023, **11**, 7345–7355.
71 K. Sumitomo, Y. Sudo, K. Kanazawa, K. Kawabata and K. Takimiya, *Mater. Horiz.*, 2022, **9**, 444–451.
72 B. Lu, S. Zhang, D. Liu, W. Jin, D. Li, Z. Liu and T. He, *Org. Chem. Front.*, 2025, **12**, 422–429.
73 K. Takimiya, S. Usui, A. Sato, K. Kanazawa and K. Kawabata, *J. Mater. Chem. C*, 2022, **10**, 2775–2782.
74 R. S. Fedorenko, A. V. Kuevda, V. A. Trukhanov, V. G. Konstantinov, A. Y. Sosorev, A. A. Sonina, M. S. Kazantsev, N. M. Surin, S. Grigorian, O. V. Borshchev, S. A. Ponomarenko and D. Y. Paraschuk, *Adv. Electron. Mater.*, 2022, **8**, 2101281.
75 A. A. Trul, V. P. Chekusova, D. S. Anisimov, O. V. Borshchev, M. S. Polinskaya, E. V. Agina and S. A. Ponomarenko, *Adv. Electron. Mater.*, 2022, **8**, 2101039.
76 W. Park, C. Yun, S. Yun, J. Lee, S. Bae, D. Ho, C. Kim and S. Seo, *Org. Electron.*, 2022, **105**, 106508.
77 K. Sambe, T. Takeda, N. Hoshino, W. Matsuda, K. Shimada, K. Tsujita, S. Maruyama, S. Yamamoto, S. Seki, Y. Matsumoto and T. Akutagawa, *J. Am. Chem. Soc.*, 2024, **146**, 8557–8566.
78 K. Sambe, T. Takeda, N. Hoshino, W. Matsuda, R. Miura, K. Tsujita, S. Maruyama, S. Yamamoto, S. Seki, Y. Matsumoto and T. Akutagawa, *ACS Appl. Mater. Interfaces*, 2023, **15**, 58711–58722.
79 Y.-C. Neu, Y.-S. Lin, Y.-H. Weng, W.-C. Chen, C.-L. Liu, B.-H. Lin, Y.-C. Lin and W. C. Chen, *ACS Appl. Mater. Interfaces*, 2024, **16**, 7500–7511.
80 X. Chen, S. Zheng, B. Liang, X. Wu, D. Wang, Yu. Dong, W. Huang, Y. Liu, X. Yu, J. Shen, S. Feng, C. Chang and W. Huang, *Chem. Mater.*, 2023, **35**, 2808–2819.
81 F. Chiarella, A. Carella, A. Cassinese and M. Barra, *J. Mater. Chem. C*, 2024, **12**, 7017–7028.
82 M. Geiger, R. Lingstädt, T. Wollandt, J. Deuschle, U. Zschieschang, F. Letzkus, J. N. Burghartz, P. A. V. Aken, R. T. Weitz and H. Klauk, *Adv. Electron. Mater.*, 2022, **8**, 2101215.
83 S. Inoue, T. Higashino, K. Nikaido, R. Miyata, S. Matsuoka, M. Tanaka, S. Tsuzuki, S. Horiuchi, R. Kondo, R. Sagayama, R. Kumai, D. Sekine, T. Koyanagi, M. Matsubara and T. Hasegawa, *Adv. Sci.*, 2024, **11**, 2308270.
84 A. L. Capodilupo, E. Fabiano, L. D. Marco, G. Ciccarella, G. Gigli, C. Martinelli and A. Cardone, *J. Org. Chem.*, 2016, **81**, 3235–3245.
85 Z. Zhou, J. Duan, L. Ye, G. Wang, B. Zhao, S. Tan, P. Shen, H. S. Ryu, H. Y. Woo and Y. Sun, *J. Mater. Chem. A*, 2020, **8**, 9684–9692.
86 L. Chand, P. Kumar, R. Tiwari, M. Kundar, S. K. Pal, V. Saxena, R. Singh and S. P. Singh, *Sustainable Energy Fuels*, 2024, **8**, 5458–5466.
87 D. Takhellambam, L. A. Castriotta, G. Zanotti, L. Mancini, V. Raglione, G. Mattioli, B. Paci, A. Generosi, M. Guaragno, V. Campanari, G. Ammirati, F. Martelli, E. Calabrò, A. Cricenti, M. Luce, N. Y. Nia, F. D. Giacomo and A. D. Carlo, *Sol. RRL*, 2023, **7**, 2300658.
88 W. T. M. Van Gompel, R. Herckens, P.-H. Denis, M. Mertens, M. C. Gélvez-Rueda, K. Van Hecke, B. Ruttens, J. D'Haen, F. C. Grozema, L. Lutsen and D. Vanderzande, *J. Mater. Chem. C*, 2020, **8**, 7181–7188.
89 S. Qin, J. Tan, J. Qin, J. Luo, J. Jin, S. Huang, L. Wang and D. Liu, *Adv. Electron. Mater.*, 2021, **7**, 2100557.
90 S. Gonzalez-Casal, R. Jouclas, I. Arbouch, Y. H. Geerts, C. van Dyck, J. Cornil and D. Vuillaume, *J. Phys. Chem. Lett.*, 2024, **15**, 11593–11600.
91 K. Tahara, Y. Ashihara, T. Higashino, Y. Ozawa, T. Kadoya, K. Sugimoto, A. Ueda, H. Mori and M. Abe, *Dalton Trans.*, 2019, **48**, 7367–7377.
92 K. Tahara, Y. Ashihara, T. Ikeda, T. Kadoya, J. Fujisawa, Y. Ozawa, H. Tajima, N. Toyoda, Y. Haruyama and M. Abe, *Inorg. Chem.*, 2020, **59**, 17945–17957.
93 T. Ikeda, K. Tahara, T. Kadoya, H. Tajima, N. Toyoda, S. Yasuno, Y. Ozawa and M. Abe, *Langmuir*, 2020, **36**, 5809–5819.
94 K. Tahara, T. Horio, T. Ikeda, K. Itamura, Y. Ozawa and M. Abe, *Organometallics*, 2025, **44**, 973–981.
95 M. C. Borrallo-Aniceto, M. Pintado-Sierra, A. Valverde-González, U. Díaz, F. Sánchez, E. M. Maya and M. Iglesias, *Green Chem.*, 2024, **26**, 1975–1983.
96 S. Koyama, H. Iguchi, S. Takaishi, G. Cosquer, S. Kumagai, J. Takeya, T. Okamoto and M. Yamashita, *Chem. Lett.*, 2019, **48**, 756–759.
97 T. Ikeda, K. Tahara, R. Ishimatsu, T. Ono, L. Cui, M. Maeda, Y. Ozawa and M. Abe, *Angew. Chem., Int. Ed.*, 2023, **62**, e202301109.
98 V. S. Vyas, R. Gutzler, J. Nuss, K. Kern and B. V. Lotsch, *CrystEngComm*, 2014, **16**, 7389–7392.

99 M. A. Khalily, H. Usta, M. Ozdemir, G. Bakan, F. B. Dikecoglu, C. Edwards-Gayle, J. A. Hutchinson, I. W. Hamley, A. Dana and M. O. Guler, *Nanoscale*, 2018, **10**, 9987–9995.
100 L. L. Levkov, N. M. Surin, O. V. Borshchev, Y. O. Titova, N. O. Dubinets, E. A. Svidchenko, P. A. Shaposhnik, A. A. Trul, A. Z. Umarov, D. V. Anokhin, M. Rosenthal, D. A. Ivanov, V. V. Ivanov and S. A. Ponomarenko, *Materials*, 2025, **18**, 743.
101 M. Ullah, R. Wawrzinek, R. C. R. Nagiri, S.-C. Lo and E. B. Namdas, *Adv. Opt. Mater.*, 2017, **5**, 1600973.
102 Y. Zhu, Y. Jiang, F. Cao, P. Wang, J. Ke, J. Liu, Y. Nie, G. Li, Y. Wei, G. Lu and S. Li, *J. Mater. Chem. C*, 2025, **13**, 11697–11706.
103 B. S. Shivaji, R. Boddula and S. P. Singh, *Phys. Chem. Chem. Phys.*, 2022, **24**, 15110–15120.
104 M. Montrone, A. Maggiore, A. Moliterni, P. Pander, M. Pugliese, A. L. Capodilupo, S. Gambino, C. T. Prontera, V. Valenzano, F. Mariano, G. Accorsi, T. Sibillano, C. Giannini, G. Gigli, A. Cardone and V. Maiorano, *J. Mater. Chem. C*, 2025, **13**, 160–176.
105 K. Tahara, A. Kobayashi, M. Fujitsuka, Y. Osakada, K. Tokunaga, T. Ikeda and M. Abe, *Organometallics*, 2024, **43**, 840–848.
106 T. Ikeda, K. Tahara, T. Kadoya, Y. Ozawa and M. Abe, *Chem. Lett.*, 2024, **53**, upae092.

